Acta Materialia 278 (2024) 120220

Contents lists available at ScienceDirect

Acta Materialia

journal homepage: www.elsevier.com/locate/actamat

Full length article

Comparison and validation of stochastic microstructure characterization and reconstruction: Machine learning vs. deep learning methodologies

Arulmurugan Senthilnathan [a,1], Vishnu Saseendran [b,1], Pinar Acar [a,*], Namiko Yamamoto [b,*], Veera Sundararaghavan [c]

[a] Department of Mechanical Engineering, Virginia Tech, Blacksburg, 24061, VA, USA
[b] Department of Aerospace Engineering, The Pennsylvania State University, University Park, 16802, PA, USA
[c] Department of Aerospace Engineering, University of Michigan, Ann Arbor, 48109, MI, USA

ARTICLE INFO

Keywords:
MRF
CNN
Deep learning
Microstructure reconstruction
Moment invariants
Polycrystalline

ABSTRACT

In the world of computational materials science, the knowledge of microstructure is vital in understanding the process-microstructure–property linkage across various length-scales. To circumvent costly experimental characterizations, typically, analyses on ensembles of 3D microstructures within a numerical framework are preferred. Utilizing a moment invariants-based physical descriptor, the current work quantifies the variations in the microstructural topology of 3D synthetic data of polycrystalline materials. For the first time, the validation of synthetic microstructures based on two unique AI-based reconstruction approaches was compared, providing valuable insights into the diverse characteristics of each methodology. Virtual 3D microstructure volumes of forged Ti-7Al and additively manufactured 316L stainless steel alloys were generated from 2D experimental data using two methods — Markov Random Field (MRF) and deep learning-based volumetric texture synthesis. Quantitative evaluation and validation of the reconstructed volumes were carried out with the aid of moment invariants by comparing local features associated with grain-level properties, such as grain size and shape. The normalized central moments previously employed to compare 2D grain topology were expanded to 3D. With the advent of various reconstruction algorithms, especially AI-based, the validation methodology outlined in this work can be adopted to evaluate the robustness of various 3D reconstruction frameworks as well as ensure spatial equivalency of the target microstructures.

1. Introduction

Owing to the high cost involved in 3D material characterization and reconstruction, advanced reconstruction methodologies are gaining popularity for synthesizing statistically equivalent 3D microstructures from 2D scans [1–7]. These techniques also play a crucial role in the rapid development and optimization of process control parameters in additive manufacturing [8]. Instead of relying solely on deterministic descriptions obtained through conventional 3D scans, the primary focus of reconstruction methodologies is to match the key statistics and characteristics of a given microstructure. To reliably establish structure–property linkage using probabilistic methods, it is vital to characterize microstructures using a fairly large dataset. Therefore, to predict mechanical or physical properties, an ensemble of microstructures that enables comprehensive statistical representation is preferred. The primary aim of a reconstruction problem is to accurately characterize the stochastic material morphology and use it to generate statistically equivalent virtual microstructure volumes.

However, it is important to note that the reconstruction techniques generate a statistically equivalent microstructure. Therefore, it is crucial to validate the reconstructed microstructure with the experimental data. However, currently, there does not exist any explicit guideline to validate the 3D synthetic microstructure volumes to the 2D experimental images, especially pertaining to polycrystalline materials that comprise complex grain topology and thus, anisotropy in grain shapes. Moreover, the existing methods do not provide a precise comparison of grain shapes in a polycrystalline microstructure [9–13]. This research gap is addressed in our previous work by developing a two-stage comparison methodology for 2D reconstruction using the concept of moment invariants [14]. In this research, we broaden the established framework designed to validate a reconstructed 3D microstructure based on a 2D experimental Electron Backscatter Diffraction (EBSD) image. Therefore, this work introduces a moment invariant-based validation procedure that is universally applicable to any reconstruction

* Corresponding authors.
E-mail addresses: pacar@vt.edu (P. Acar), nuy12@psu.edu (N. Yamamoto).
[1] These authors contributed equally to this work.

https://doi.org/10.1016/j.actamat.2024.120220
Received 13 February 2024; Received in revised form 11 June 2024; Accepted 24 July 2024
Available online 31 July 2024

approach. We demonstrate this framework on two distinct AI-based reconstruction algorithms by employing exemplars of both conventional forged and additively manufactured polycrystalline materials.

The microstructure reconstruction approaches in the literature may be broadly classified as statistical modeling-based [1], visual features-based [2] and machine learning-based [3]. In this work, two distinct reconstruction algorithms from the field of machine learning and texture synthesis are considered. The first one is a conventional texture synthesis approach known as the Markov Random Field (MRF) [15], and the next is a modern Convolutional Neural Networks-based (CNN) volumetric texture synthesis approach [16]. To the authors' best knowledge, the MRF-based and CNN-based models have not yet been compared and validated. Furthermore, for the first time, this CNN-based texture synthesis model is applied to synthesize virtual volumes of anisotropic polycrystalline materials.

The idea of texture synthesis originated in the computer graphics community, wherein the 2D experimental images have been employed for the generation of synthetic 2D or 3D images [17–21]. The texture synthesis approach is efficient due to it being image-based (and thus, material agnostic) and this method is known to preserve materials descriptors, especially higher-order correlation functions that cannot be achieved via lower-order feature optimization-based approaches. MRF-based texture synthesis model, in particular, is based on the use of a high-order Ising structure [22] to represent an image of $N \times N$ pixels as $N \times N$ lattice structure. Over the constructed Ising model, a Markov property is applied, and it states that the probability of a pixel coloring (X) is conditionally independent of all other values in the lattice structure, except its neighbors. The MRF algorithm generates synthetic images by sampling the probability distributions learned from a few 2D exemplars [15]. The algorithm has been extended to the modeling of 3D anisotropic materials [23] from 2D exemplars through an optimization-based approach. There are multiple advantages to considering the MRF algorithm for microstructure reconstruction. Due to the random nature of the algorithm, multiple 3D microstructures can be generated from the same input seed image. Moreover, synthetic microstructures generated by MRF are a valuable source for exploring the variations associated with the inherently random nature of polycrystalline microstructures. Additionally, the MRF algorithm requires only a small portion of the experimental data to reconstruct large spatial domains for anisotropic microstructures [24]. Therefore, MRF is considered one of the candidates in this work to perform the 3D reconstruction of polycrystalline materials.

On the other hand, with the advent of AI-based materials discovery, CNNs are increasingly gaining popularity due to their excellent suitability for handling image data [11,25–33]. The machine learning (ML)-based reconstruction approach may be further classified as material-system dependent and material-system independent [11]. In a material-system dependent approach, the weights of the employed network are trained with images specific to the material under consideration [34,35], necessitating retraining of these weights for new materials. Conversely, transfer learning approaches, another class of ML-based methods, are material-system independent and circumvents the need to train weights with a set of materials data [11,26,27]. Note that such deep learning models employ pre-trained weights from computer vision datasets. For instance, activations of network layers of deep CNN model, VGG-19 [36] trained on ImageNet database [37] are employed to synthesize reconstructions of a target microstructure [11,27,28]. It should be noted that such model may still require hyperparameter tuning to yield optimal results. In the field of computer vision and graphics, Solid Texture Synthesis (STS) methods [38,39] are commonly used to synthesize solid textures across a set of slicing directions for a given 2D exemplar [40–42]. The STS method adds texture to a 3D surface by evaluating a colormap function at specified coordinates in 3D space. For instance, 3D texture solids are synthesized from 2D exemplars using a non-parametric texture optimization approach coupled with histogram matching [40]. This method successfully addresses the ill-posed nature of the problem, assuming that the exemplar is a stationary texture with spatial locality, and has been applied to model 3D microstructures of natural materials and porous media [17,19,20,43–45].

Recent advancements in machine learning have led to the introduction of a novel on-demand volumetric texture synthesis framework based on deep learning [16]. Based on a perceptual slice-based loss function, this proposed framework of STS adopts a compact generative network that takes a multi-scale noise input and produces a 3D solid texture. This advanced CNN-based model is capable of generating highly realistic solid textures of arbitrary size and has shown great potential in generating high-quality 3D microstructures [46–50]. To the best of our knowledge, the application of deep learning-based texture synthesis models for reconstructing microstructures in additively manufactured materials that have complex grain structures remains unexplored. Moreover, the statistical equivalence of the generated microstructures using this deep learning-based approach against conventional texture synthesis using MRFs needs to be validated using a metric that is invariant to translation, scale, and rotations of the complex grain shapes.

A brief note is made here on another prominent class of deep learning method, Generative Adversarial Network (GAN) [51], which has found profound applications in microstructure reconstruction [52–58]. The GAN-based algorithms attain Nash equilibrium between the generator and discriminator which achieves superior generative performance through adversarial training. Although GAN-based microstructure reconstruction algorithms have been used to successfully generate synthetic microstructures of a variety of materials such as porous media [53,55,59,60], solid oxide fuel cell electrodes [56], and polycrystalline materials [61,62], they are vulnerable to a condition known as mode collapse [63], which results in these models generating images with insufficiently diverse (or limited) features. A few other challenges of the GAN-based models include the adversarial nature of the loss function owing to unstable training, and the non-interpretability of the model's latent space [64–67]. To overcome these challenges, especially the mode collapse, GANs are often combined with other machine learning models to obtain the so-called hybrid models. For instance, Variational Encoders (VAEs) [68], a special class of autoencoders when combined with GANs appear promising [67,69,70].

Other prominent microstructure characterization and reconstruction approaches include Bayesian and diffusion-based models. The former is a sample-efficient method capable of finding optimal solutions, especially in the context of finite and noisy data, whilst the latter circumvents adversarial training methods that are known for common GAN training issues. The Bayesian reconstruction problem is formulated as finding a solution that has the highest probability of being correct in the light of observed data and a given exemplar [71]. In addition to reconstruction of 3D porous structures [72], architected [73], and polycrystalline materials [74], Bayesian method has also been successfully applied in electron cryo-microscopy [75,76], reconstruction of current densities [77] as well as magnetic resonance imaging [78]. Diffusion models, on the other hand, avoid the adversarial training methods by incrementally adding small amounts of noise to training images and learn a reverse diffusion process to generate structured data from random noise [79]. The diffusion-based models have been successfully applied for the reconstruction of a wide array of microstructures such as polycrystalline, ceramics, fiber composite, powder and porous sponge, fractal noise materials, and so on [79–84]. Nonetheless, with the rise of several machine learning-based microstructure reconstruction algorithms, it is vital to have a framework to benchmark and validate the synthesized data. In this work, we propose to establish such a framework that enables materials engineers to validate their AI-generated synthetic 3D data against the ground-truth by utilizing synthetic microstructure data reconstructed with CNN and MRF methods.

The complexity of microstructure, especially in polycrystalline materials makes it difficult to characterize and quantify the grain shapes. Traditionally quantitative measures for validating the reconstructed microstructure with the target image include comparing them visually [85] or through the grain sizes [11]. Nevertheless, to compare different reconstruction algorithms and quantify complex grain shapes, the use of a physical or geometric-based descriptor becomes essential. It has been demonstrated that a comprehensive characterization of 3D reconstructed grains is required at both global and local levels [14,86]. In the past, well-known shape descriptors and measures such as the two-point correlation [1], shape quotient [87,88], visual inspection [11], and histogram matching [19,89] were used to validate the reconstructed microstructures. However, through moment invariants, we can achieve explicit quantification of grain shapes as they remain invariant to translations, scales, and rotations of the grain shapes. Therefore, moment invariant is the preferable metric to validate the synthetic microstructures with the experimental data. Previously, the moment invariants are introduced by [90–92] to characterize and classify the precipitates and powder particles. However, the authors introduced the two-stage moment-invariant approach for 2D to 2D validation [86] that can be applied to any type of microstructures. This work extends the validation procedure from 2D to 3D, and employs moment invariants for the comparison and validation of the synthetic microstructures generated by two distinct AI-based microstructure reconstruction algorithms — MRF and CNN-based models. The texture and grain topology of computationally reconstructed 3D microstructures using the two algorithms are examined on two distinct material systems fabricated through various techniques. The first material is additively-manufactured 316L stainless steel, while the second is conventionally forged Ti-7Al alloy.

2. Methods overview

2.1. MRF-based microstructure reconstruction

The input to the MRF microstructure reconstruction algorithm consists of three orthogonal planar exemplars, whereas the output is a 3D solid structure containing voxels that are colored consistently with input orthogonal exemplars. The details of the 3D reconstruction from 2D images using the MRF technique as originally described in Javaheri and Sundararaghavan [23,24] is briefly summarized below. Let $\boldsymbol{S}^i$ for $i = \{x, y, z\}$ denote a set of three orthogonal microstructural exemplars along the respective i axis. The symbol $\boldsymbol{V}$ indicates the synthesized 3D microstructure, with $\boldsymbol{V}_v$ representing the RGB coloring of the voxel v. The vector denoting the spatial neighborhood of voxel v in the slice orthogonal to the i axis, as illustrated in Fig. 1(a), is denoted by $\boldsymbol{V}^i_v$ where $i = \{x, y, z\}$. Additionally, let $\boldsymbol{S}^{i,w}$ denote a window of the same size in the respective 2D micrographs $\boldsymbol{S}^i$. Based on the Markovian assumption, the Probability Density Function (PDF) for RGB coloring of a voxel given the states of its spatial neighborhood is independent of the entire dataset. Accordingly, the most likely RGB triplet of the voxel v can be estimated by identifying the center pixel values of windows $\boldsymbol{S}^{i,w}$ in the 2D input exemplar that best resembles the corresponding $\boldsymbol{V}^i_v$ cross-sections. These windows, as seen in Fig. 1(b), are denoted as $\boldsymbol{S}^i_v$ for $i = \{x, y, z\}$.

Subsequently, the RGB coloring of voxel u in the neighborhood $\boldsymbol{V}^i_v$ is denoted as $\boldsymbol{V}^i_{v,u}$. Let the values $\boldsymbol{S}^i_{v,u}$ and $\boldsymbol{S}^{i,w}_u$, respectively denote the RGB triplets of pixel u in the windows $\boldsymbol{S}^i_v$ and $\boldsymbol{S}^{i,w}$. Consequently, the 3D solid microstructure can be synthesized by posing the reconstruction problem as an optimization of the energy function formulated below:

$$E(\boldsymbol{V}) = \sum_{i\in\{x,y,z\}} \sum_v \sum_u \omega^i_{v,u} \|\boldsymbol{V}^i_{v,u} - \boldsymbol{S}^i_{v,u}\|_2^2 \tag{1}$$

where $\|.\|_2$ denotes the L_2 norm, and $\omega^i_{v,u}$ represents per-pixel radially-symmetric weighting factors based on a Gaussian distribution. The optimization of the energy function, $E(\boldsymbol{V})$, as outlined in Eq. (1), is carried out in three steps: (*i*) searching step, (*ii*) expectation step, and (*iii*) histogram matching step. Consequently, within the first step, the best-matching neighborhood of voxel v, $\boldsymbol{S}^i_v$, in each orthogonal planer image is selected by solving the following optimization problem:

$$\boldsymbol{S}^i_v = \arg\min_{\boldsymbol{S}^{i,w}} \sum_u \omega^i_{v,u} \|\boldsymbol{V}^i_{v,u} - \boldsymbol{S}^{i,w}_u\|_2^2 \tag{2}$$

The searching step outlined in Eq. (2) consists of an exhaustive process that compares all the windows in the input 2D exemplars, $\boldsymbol{S}^{i,w}$, to the corresponding neighborhood of voxel v, $\boldsymbol{V}^i_v$, and identifies windows, $\boldsymbol{S}^i_v$, that lead to a minimum weighted squared Euclidean distance. Generally, the center pixel values in $\boldsymbol{S}^i_v$ for $i = \{x, y, z\}$ are composed of distinct RGB triplets. Yet, an optimal value of $\boldsymbol{V}_v$ needs to be inferred by weighting colors pertaining to location v not only in the matching windows of voxel v but also in its surroundings, as follows:

$$\boldsymbol{V}_v = \sum_{i\in\{x,y,z\}} \sum_u \omega^i_{u,v} \boldsymbol{S}^i_{u,v} \Big/ \sum_{i\in\{x,y,z\}} \sum_u \omega^i_{u,v} \tag{3}$$

Note that in the expectation step, the subscripts u and v are switched in Eq. (3), compared to Eq. (2). This implies that the optimal color of the voxel v, $\boldsymbol{V}_v$, is the weighted average of the colors at locations corresponding to voxel v in the best-matching windows of voxels u found within the synthesized 3D microstructure. The RGB channels here are averaged independently in Eq. (3). Since $\boldsymbol{V}_v$ is continuously changing after each step, the set of closest input neighborhoods $\boldsymbol{S}^i_v$ may vary accordingly after each iteration. Hence, the above two steps are repeated until convergence; that is until the set of $\boldsymbol{S}^i_v$ remains unchanged.

Furthermore, the color space associated with micrograph images is typically discrete and range-bound. Consequently, the averaging performed in Eq. (3), always tends to shrink the color levels. For instance, the color level 0 has the tendency to increase, due to it being averaged with all the color levels that are greater or equal to 0. However, the assumption in MRF reconstruction remains that the two datasets (*i.e.*, three orthogonal planar exemplars and solid synthesized model) have the same Cumulative Distribution Function (CDF) of color densities. As a result, given the reference exemplars and the target synthesized images, the MRF algorithm normalizes the color histograms at the end of each iteration by first binning the colors into 255 discrete intervals. Thereafter, histogram matching is applied independently for each RGB color channel such that the color density of the synthesized model closely matches with the planar exemplars. The methods are implemented in the Windows executable with a graphical interface 'MRFVoxel', whose inputs are the three orthogonal images and output is the 3D microstructure.

2.2. CNN-based microstructure reconstruction

The details of the CNN-based generative network employed in this work as originally described by Gutierrez et al. [16] is briefly presented here. In this solid texture synthesis model based on a deep learning framework, a compact CNN generator produces a solid texture from a multi-scale 3D noise input, $Z = \{z_0, \ldots, z_K\}$. As illustrated in Fig. 2 on a conventionally forged Ti-7Al sample, a convolutional neural generator, $\mathcal{G}$, is trained to synthesize the solid texture, $v = \mathcal{G}(Z|\theta)$, with statistical features akin to the target exemplar through convolution, concatenation and upsampling operations from the multi-channel 3D white noise inputs, Z. Through a multi-scale architecture of convolution, concatenation, and upsampling operations, the compact generative network converts the white noise, Z, to a solid texture, v. This process starts at the coarsest scale in which the volumetric noise sample, Z, is processed with a set of convolutions and upsampling operations to reach the next level. Here it is concatenated with another independent noise sample from the next scale that is also treated with a set of convolutions. Note, that this proposed generative network, $\mathcal{G}$, is capable of synthesizing rectangular texture volumes of any arbitrary

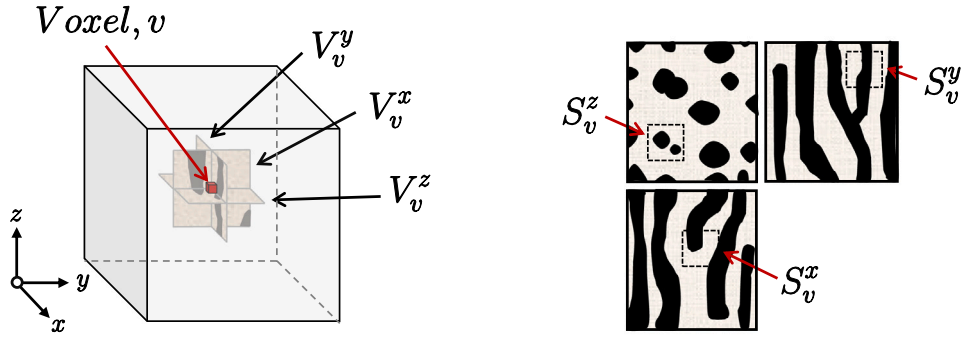

(a) MRF 3D Synthesized Model (b) Orthogonal Planar Images

Fig. 1. MRF reconstruction schematic: (a) the neighborhoods of the voxel v along the orthogonal axes, denoted as $\boldsymbol{V}_v^i$ for $i = \{x, y, z\}$, are shown. (b) The windows in the input 2D micrograph shown in dotted lines are denoted by $\boldsymbol{S}_v^i$. These windows closely resemble the cross-sectional neighborhoods of the voxel, $\boldsymbol{V}_v^i$.

size and is driven by the size of the exemplar(s). Here we employ this CNN-based model to synthesize rectangular volumes of the two distinct polycrystalline material systems (Ti-7Al and 316L SS).

During training, the generator parameters (θ), namely, the weight, mean, bias, and variance of the batch normalization layers in the concatenation, and bias and kernels of the convolution block are learned by the model. The synthesized volumes, $v = \mathcal{G}(Z|\theta)$, are then compared to the target exemplar(s) $\{u_1, \ldots, u_D\}$ corresponding to the desired view along $D \in \{1, 2, 3\}$ directions among the three canonical directions of the Cartesian grid. This is attained with the aid of a slice-based perceptual loss function by comparing the feature map, F, of the 2D slices, $\boldsymbol{v}_{d,n}$ (nth slice along dth direction of the solid) with the exemplar, $\boldsymbol{u}_d$. Note, that the constrained slice directions can also be controlled to enable the generator to consider various orthogonal directions allowing the model to handle anisotropic solid textures. The feature maps, F, of the exemplar, u_d, and the extracted 2D slices, v_D^n, from the generated solid microstructure are obtained from the pre-trained network deep CNN descriptor network, VGG-19 [36]. Note, that the feature maps, F, are intermediate outputs in a deep CNN model. The volumetric slice-based loss function utilizing the Gram matrix, G, measures the difference in textures of the exemplar and the 2D slices extracted from the synthesized volume. The Gram matrix, $\boldsymbol{G}_{i,k}^l = \sum_k F_{i,k}^l F_{j,k}^l$, correlates how similar the feature map, $\boldsymbol{F}_{i,k}^l$ is to its transpose, $F_{j,k}^l$; where l = number of layers, k = number of channels. When the feature vectors get more similar, the dot product ($\boldsymbol{G}_{i,k}^l$) gets larger. Hence, the Gram matrix, G, with the aid of feature maps (represented as VGG statistical features of the microstructure), enables an understanding of how well correlated the textures of the exemplar and the 2D slices extracted from the synthesized 3D microstructure are. On training, the generator learns to synthesize solid textures by minimizing the 2D perceptual loss function [16,93], defined as:

$$Loss = \sum_{l \in L} \left\| \boldsymbol{G}^l\left(\boldsymbol{F}^l(v_{d,n})\right) - \boldsymbol{G}^l\left(\boldsymbol{F}^l(u_d)\right) \right\|_2^f \tag{4}$$

where $\|\cdot\|_f$ is the Frobenius norm, u_d denotes the 2D exemplar(s), and $v_{d,n}$ denotes the slices of the synthesized 3D microstructure. For the 3D microstructure, $v \in \mathbb{R}^{r \times h \times w \times 3}$ (4D tensor of size — thickness, height, width and three-channel, *i.e.*, RGB), v_D^n is given as the nth 2D slice of the generated solid orthogonal to the dth direction. Such a volumetric slice-based loss function definition in Eq. (4) leads to memory-efficient training, and enables the utilization of high-resolution 2D micrographs as input images. In the traditional CNN-based optimization approach, several batches of virtual volumes need to be synthesized which require exorbitant memory allocation. Hence, the computational complexity and memory limitations are overcome by comparing only 2D slices, v_D^n, of the synthesized solid with the exemplar(s), u_d. During training, the parameters are optimized using the Adam algorithm [94] with an initial learning rate of 0.1 over 3000 iterations. In addition, for all the reconstructions in this study, a multi-step scheduler was employed which decayed the learning rate by a factor 10 at pre-set epochs 300, 1000 and 2000. Moreover, this framework may be easily adapted to input grayscale images (single-channel) without any significant modification [46,50]. Fig. 3 shows the estimation of loss function during training of two material systems considered in this study. With three slicing directions, training was performed using one GPU NVIDIA Quadro RTX 5000. In general, visual convergence occurred after 1500 iterations, see Fig. 3. The resolution of the samples was 128^2 and 100^2 pixels for 316L SS and Ti-7Al, respectively.

2.3. Moment invariants

An image is a discrete function (I) that has pixel intensity values ranging from 0 to 255. A moment of an image can be described as an average weightage number based on the pixel intensity values and its corresponding location in a Cartesian coordinate. For brevity, a few types of moments and their invariants are discussed here. More information on the concept of moment invariants is available in the author's previous work [14]. A basic type of moment is called the raw moment (m) which is defined as:

$$m_{ij} = \sum_x \sum_y x^i y^j I(x, y) \tag{5}$$

where $i, j = 0, 1, 2$ represents the order of the moment. The basis functions x and y denote the coordinates of the pixel intensity. Moment invariants are initially introduced by Hu [95]. Each type of invariant generates a value for a given discrete function (I) that remains constant for various shape transformations. For example, central moments (μ) remain invariant to the translation of shapes. They are formulated as:

$$\mu_{pq} = \sum \sum (x - \bar{x})^p (y - \bar{y})^q I(x, y) \tag{6}$$

where p and q represent the order of the moments and $\bar{x}$ and $\bar{y}$ (Eq. (7)) denote the centroid of an image, defined as the ratio of the 1st-order raw moment to the 0^{th}-order raw moment.

$$\bar{x} = \frac{m_{10}}{m_{00}}, \qquad \bar{y} = \frac{m_{01}}{m_{00}} \tag{7}$$

When the central moments are divided over the image area (A) to the power of $\gamma = (\frac{p+q+2}{2})$, a normalized central moment (η) is created. The formulation of η is presented as:

$$\eta_{pq} = \frac{\mu_{pq}}{A^\gamma} \tag{8}$$

The normalized central moment (η) is invariant to both the translation and scale of shapes. The formulation for η values of 3D can be extrapolated from Eq. (8). Furthermore, η statistically represents the normalized variance of the pixel intensities in a particular direction. For example, both the η_{20} for a 2D image and η_{200} for a 3D microstructure

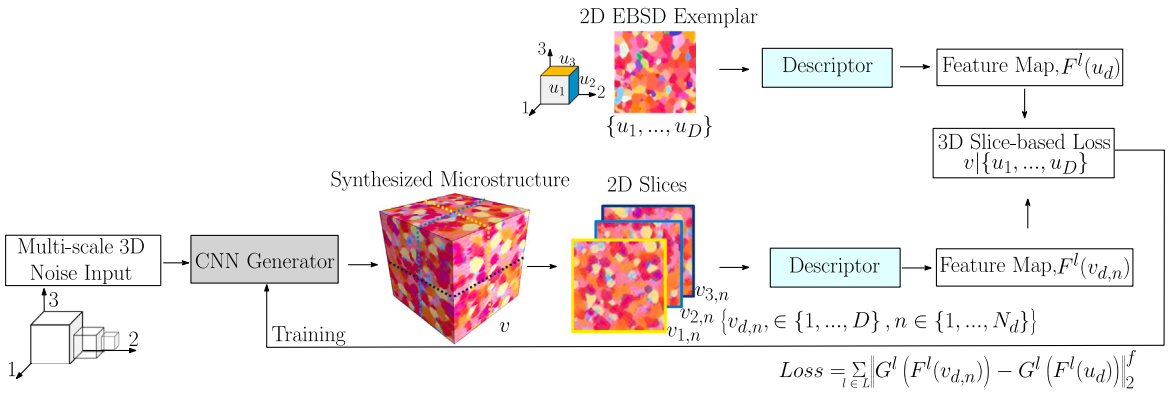

Fig. 2. Deep learning-based training framework illustrated on a conventionally forged Ti-7Al material sample, where the CNN generator, $\mathcal{G}(Z|\theta)$, synthesizes the microstructural volume, v from a 3D multi-scale noise input, $Z = \{z_0, \ldots, z_K\}$. The slice-based perceptual loss function compares the statistical features of the exemplar, u_d, with 2D slices of the generated microstructure, v_D^n. Pre-trained deep CNN, VGG-19 is employed here as the descriptor network.
Source: Adapted with permission from [16].

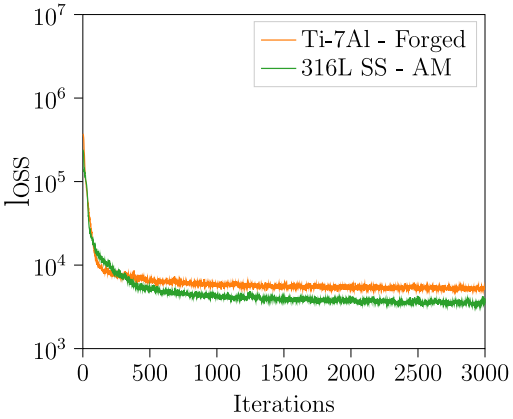

Fig. 3. 3D empirical loss during generator training for exemplars — Additively Manufactured (AM) 316L Stainless Steel and conventionally forged Ti-7Al alloy.

represent the normalized variance of pixel intensities/voxel values in the x direction. Therefore, η is a good candidate to compare both 2D and 3D two microstructures of different dimensions. Using η for verifying the 3D synthetic microstructures from 2D images was first introduced in our previous work [96]. Here, the verification procedure is extended for studying and validating the two AI-based microstructure reconstruction techniques.

Two types of microstructures are used in this work to statistically verify the 3D synthetic microstructures obtained from 2D images via the two distinct reconstruction algorithms. Each case contains microstructures of different materials and manufacturing procedures. Detailed information on the two cases is provided in Fig. 2. Each grain in the experimental 2D images and synthetic 3D microstructure is individually separated and quantified by η. An example of clusters of grains separated from the 3D microstructure is presented in Figs. 5 and 6.

3. Results

The reconstruction methodologies were investigated in this work using two distinct experimental material systems via EBSD (Electron Back Scattering Diffraction) images obtained at oblique angles. A conventionally forged Ti-7Al 2D image and a set of three orthogonal additively manufactured 316L stainless steel 2D images were used for studying the isotropic and anisotropic reconstructed virtual microstructures. Fig. 4 shows the 3D reconstructed microstructures alongside respective exemplars utilized in this analysis. The statistical resemblance of the reconstructed microstructures to the experimental images is analyzed both qualitatively and quantitatively.

The objective of the qualitative analysis is to compare the visual similarity of the reconstructed virtual microstructures to the experimental microstructures. Due to the inherent difference in grain structure between additively manufactured and forged samples, first, visual analysis was conducted to evaluate the capability of each algorithm in capturing the topology of the clusters. Although visual comparison is not a strong candidate to validate a synthesized microstructure, many studies [11,27] in the literature have employed it to conduct a preliminary analysis of the performance of the reconstruction algorithm. Therefore, first, the quality of the reconstruction algorithms is analyzed by observing the presence of the same orientations (colors) in the experimental and synthesized microstructures. Visually, a similarity in the colors representing the crystallographic orientations between the reconstructed and experimental microstructures is observed for both cases in Fig. 4. However, visual comparison is not sufficient to validate the synthesized microstructures. Therefore, it is crucial to quantitatively validate the synthetic microstructure with respect to the experimental microstructure by using statistical metrics.

The most commonly used features for comparing two microstructures are grain size and orientation [27]. However, the texture of a microstructure is imparted through the shapes of its grains. Furthermore, grain shape influences the macro-scale mechanical properties. Therefore, it is crucial to compare the 3D microstructures to the experimental images with respect to the grain shapes. Hence, the grain shapes of the 2D exemplar and the 3D synthetic microstructures are quantitatively compared here with the aid of moment invariants.

For the quantitative analysis, the normalized central moments (η) as formulated in Eq. (8) are used to validate the synthetic 3D microstructures with the 2D experimental microstructure images. First, the k-means clustering algorithm is used to identify the unique orientations in the microstructure. The number of 'k' values here refers to the number of unique orientations (quantified through pixel intensity values) in the microstructure. The pixel intensity values in the EBSD microstructure represent the crystallographic orientation through the Euler angles obtained experimentally with the inverse pole figure (IPF) technique. Ideally, if the number of unique orientations is known, it is not challenging to execute the k-means algorithm. However, it is hard to numerically estimate the total number of unique orientations in a microstructure image or 3D volume. Therefore, in this work, through the trial and error method, the 'k' value is obtained to be 10. This implies there are 10 unique orientations in the experimental microstructures and it is expected to observe the same orientations in the synthesized microstructure. Figs. 5 and 6 depict the clusters of Ti-7Al and the 316L stainless steel, respectively. Each cluster contains a collection of grains with the same orientation. Figs. 5(a) and 6 (a) represent

Material	Exemplar(s)	MRF-based Reconstruction	CNN-based Reconstruction
Ti-7Al Alloy		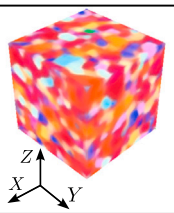	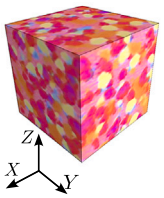
316L Stainless Steel	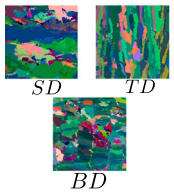	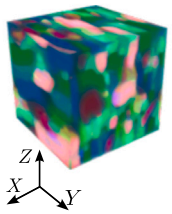	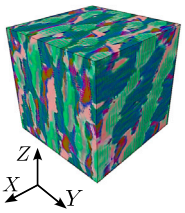

Fig. 4. Qualitative assessment — Comparison of 3D reconstructed microstructures and their respective exemplar(s); Ti-7Al Alloy (conventionally forged) and 316L SS (additively manufactured) synthesized using both MRF-based and CNN-based reconstruction methodologies. In the anisotropic case, the SD, BD, and TD refer to the Scanning, Building, and Tangential Directions, respectively, corresponding to the X, Y and Z directions in 3D Cartesian coordinate system.

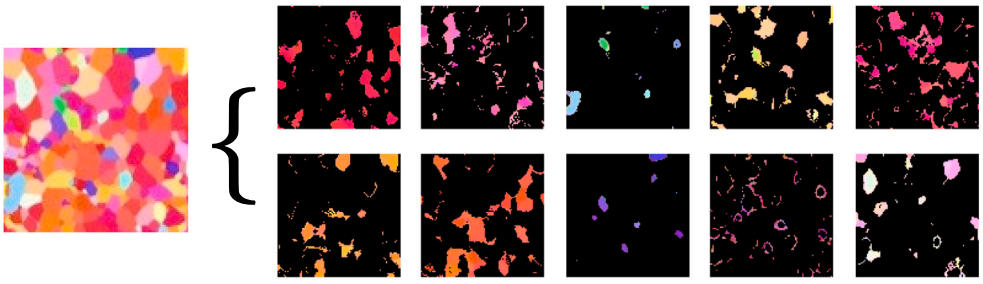

(a) Grain clusters of the conventionally forged experimental microstructure.

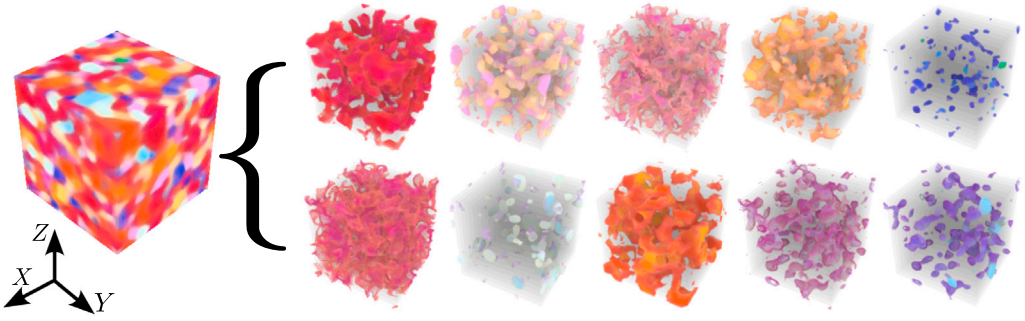

(b) Synthesized 3D microstructure and grain clusters from the MRF model.

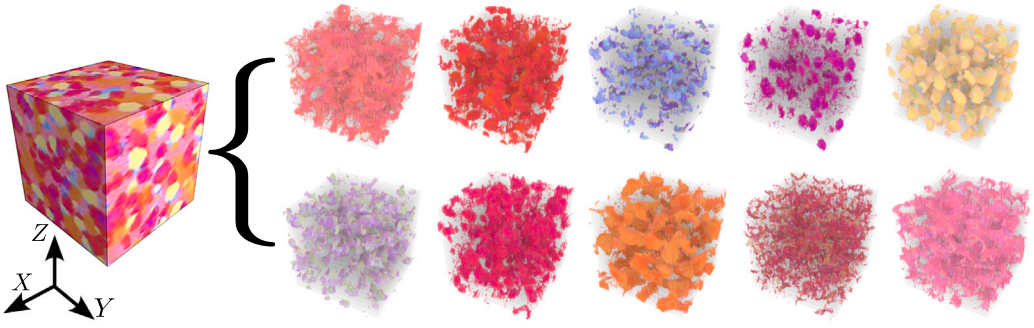

(c) Synthesized 3D microstructure and grain clusters from the CNN model.

Fig. 5. Clusters consisting of grains with the same orientation in the experimental and synthesized 3D microstructures of conventionally forged Ti-7Al sample. Each grain in every cluster is individually separated and quantified through η.

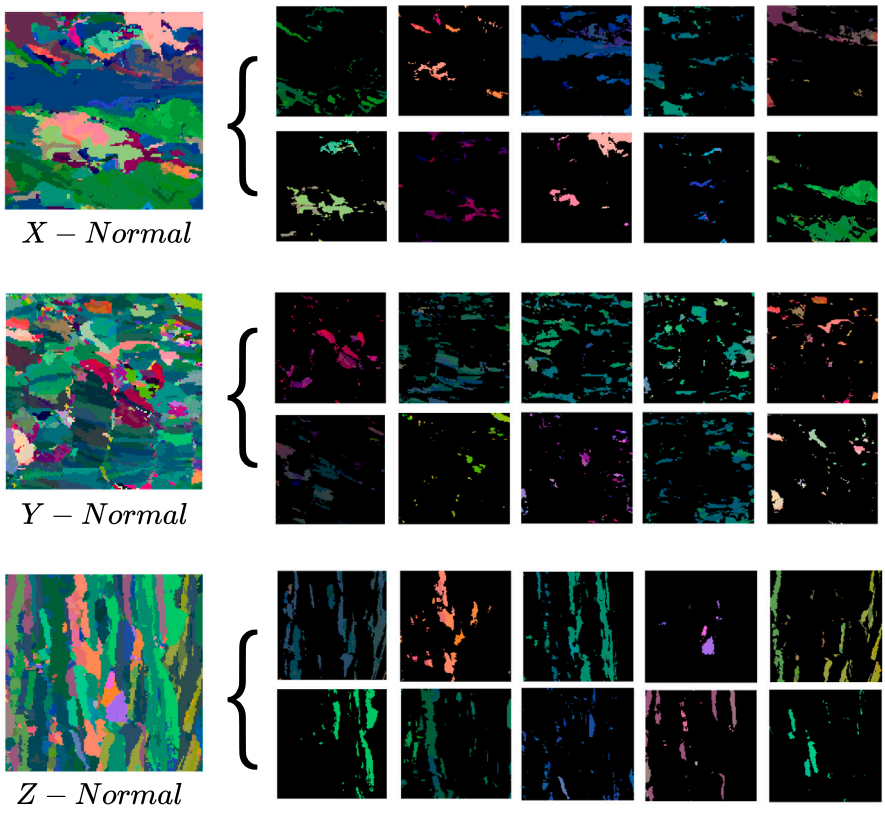

(a) Grain clusters from exemplar(s) along X, Y and Z-normal directions.

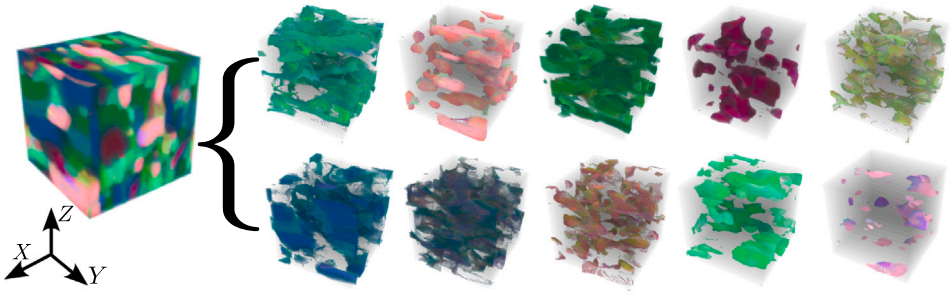

(b) Synthesized 3D microstructures using MRF model.

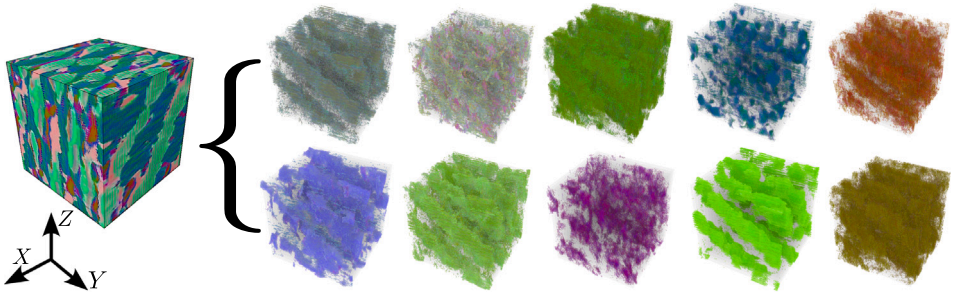

(c) Synthesized 3D microstructures using CNN model.

Fig. 6. Clusters consisting of grains with the same orientation in reconstructed microstructural volumes, additively manufactured 316L stainless steel. Each grain in every cluster is individually separated and quantified through η.

the clusters extracted from the conventionally forged and additively manufactured experimental images, respectively. Each grain in both 2D and 3D microstructural clusters is separated and quantified with the normalized central moments (Eq. (8)). The statistical equivalence of the experimental and synthetic grain shapes are then compared by plotting the normalized moments, $|ln\eta|$, in box whisker charts. The developed procedure is tested on both MRF (Section 2.1) as well as CNN-based (Section 2.2) reconstructed microstructures for both material systems.

The 2D and 3D grains quantified with η are then compared to each other through a set of box-whisker plots presented in Figs. 7 and 8. In Fig. 7, for the isotropic reconstruction of the Ti-7Al sample, the η values of 2D grains measuring the normalized variance in horizontal (H) and

Table 1
Mean and variance of the 3D reconstructed grain shape distribution quantified by $|ln\eta|$ for the conventionally forged microstructures. The mean and variance of 2D conventionally forged experimental grain shape distribution is 5.39 and 3.47, respectively.

Mean Cases	X-Normal Plane	Y-Normal Plane	Z-Normal Plane
MRF Model	8.80	8.77	8.89
CNN Model	8.29	8.19	8.58
Variance			
MRF Model	0.87	0.79	0.83
CNN Model	0.98	1.02	0.96

Table 2
Mean and variance of the 3D reconstructed grain shape distribution quantified by $|ln\eta|$ for the additively manufactured microstructures.

Mean Cases	X-Normal Plane	Y-Normal Plane	Z-Normal Plane
Experiment	5.22	5.17	5.25
MRF Model	7.60	9.36	8.40
CNN Model	5.06	4.73	3.89
Variance			
Experiment	2.77	2.95	3.34
MRF Model	1.79	1.57	1.77
CNN Model	0.84	3.14	1.39

vertical (V) directions are compared with resolved X, Y, and Z directions of each 2D plane. In the case of anisotropic reconstruction of 316L stainless steel sample, the η values of 2D and 3D grains representing the normalized variance in X, Y, and Z directions are compared with each other and plotted in Fig. 8. The line that divides the box in Figs. 7 and 8 denotes the median of the grain shape distribution quantified by η. Furthermore, the alignment of the median line towards a side (top or bottom) indicates how the skewness of the grain shape distribution is orientated. The outliers in Figs. 7 and 8 denote the unusually shaped grains. Furthermore, the mean and variance of $|ln\eta|$ distribution for both cases have been computed and presented in Tables 1 and 2.

4. Discussion

Different metrics are defined to validate the 3D synthetic microstructures with respect to the 2D experimental microstructures based on Figs. 7 and 8, as presented next:

- **Mean and variance**: From Table 2, it is observed that the mean of the grain shape distributions for the CNN reconstructed microstructures is closer to the mean of the experimentally observed microstructures than the MRF generated samples. This implies that the CNN algorithm performed better than the MRF for the additively manufactured case. This concludes that the uncertainty propagation from the experimental microstructure is more significant for the MRF samples than the CNN samples. However, the variance values (Table 2) of the MRF reconstructed 3D grain shapes are closer to the values associated with the experimental 2D grain shapes compared to the CNN samples except for the Y-normal plane. Furthermore, the mean and variance (Table 1) of the grain shape distributions for both algorithms are similar for conventionally forged cases. Therefore, mean and variance alone may not be sufficient to distinguish which algorithm performs better. Moreover, the variance alone is also not a good metric to compare two distributions, especially when the mean is shifted. Hence, a box whisker plot is necessary to identify and analyze the best-performing algorithm as well as compare the distributions of the grain shapes.
- **Outliers**: In the conventionally forged case, more outliers are observed for the MRF reconstructed 3D microstructures than the CNN, except for the grain shape distribution in the Y direction of Z-normal plane (see Fig. 8). This implies that more unusually shaped grains are present in the MRF-reconstructed conventionally forged 3D microstructure. These unusually shaped grains do not resemble the grains in the 2D experimental microstructure. However, for the additively manufactured case, the outliers were more for the CNN reconstructed 3D microstructure than the MRF. The comparison of outliers here infers that the MRF can handle the anisotropic reconstruction better than CNN.
- **Median**: Median values collectively describe the entire dataset better than the mean values. For both cases, Figs. 7 and 8 denote that the median of the grain shapes in the CNN reconstructed microstructures was close to the grain shapes in the experimental microstructures than MRF except for z_{3D}.

An overall comparison of the two presented algorithms based on the afore-mentioned metrics indicates that the MRF algorithm worked well for the additively manufactured microstructure and the CNN algorithm worked well for the conventionally forged microstructure case. Note that the metrics presented here serve as an effective evaluation tool to compare the performance of two prominent AI-based microstructure reconstruction algorithms and validate the 3D synthesized microstructures with respect to the 2D experimental counterparts.

The reason for the better performance of the MRF in the case of additively manufactured microstructure can be attributed to the spread of the unique variables in the input image. An image is a matrix where each element has a pixel intensity value that lies between 0 to 255. Therefore, the total number of possible pixel intensity values for an image is 256. However, the 2D conventionally forged experimental image (Fig. 4) has 243 unique pixel intensity values spread over a 100×100 image. Whereas the X-normal, Y-normal, and Z-normal 2D additively manufactured experimental images (Fig. 4) have 17, 32, and 18 unique values, respectively, spread over even a larger image area of size 128×128. Meanwhile, contrary to the global optimization methods, during optimization, the CNN model seeks a 3D texture that is as close as possible to the exemplar without requiring a perfect match. For the forged case, by constraining $D = 3$ (the three canonical directions of the Cartesian grid), a high number of unique pixel intensity values enabled the generator to produce a 3D texture along those directions.

A major challenge of texture synthesis algorithms, or in general, for any reconstruction algorithm is to provide a solution to the field of view vs. resolution dilemma. Note that currently there does not exist any guideline for the selection of exemplar window size for a given resolution. Although the current deep learning-based generative framework exhibits computational efficiency, one notable shortcoming concerning the reconstruction is when utilizing small exemplars. This may be attributed to the descriptor network (refer to Fig. 2) that is pre-trained using larger images. For instance, the pre-trained deep CNN model used here, namely, VGG-19 is trained on the ImageNet dataset [37] that contains ~14M annotated images according to the WordNet hierarchy, with an average image resolution of 469×387 pixels. In addition, the checker-board effects that are characteristic of the texture-based reconstruction approach exist here too, and contribute to the outliers in Figs. 7 and 8. To remove this artifact, one may add a weighted term to the loss function (Eq. (4)) which is determined via trial and error. The fixed field of VGG-19 also limits the description of extremely small microstructure information contained in the experimental images which leads the CNN-model to lose this information during training. The influence of pre-trained descriptor networks, especially, lightweight non-VGG architectures on microstructure reconstruction applied to polycrystalline materials remains unexplored and is beyond the scope of current work. It is hypothesized that utilizing deep CNN architectures with improved top-1 accuracy containing residual connections will help reduce the outliers besides providing higher computational efficiency.

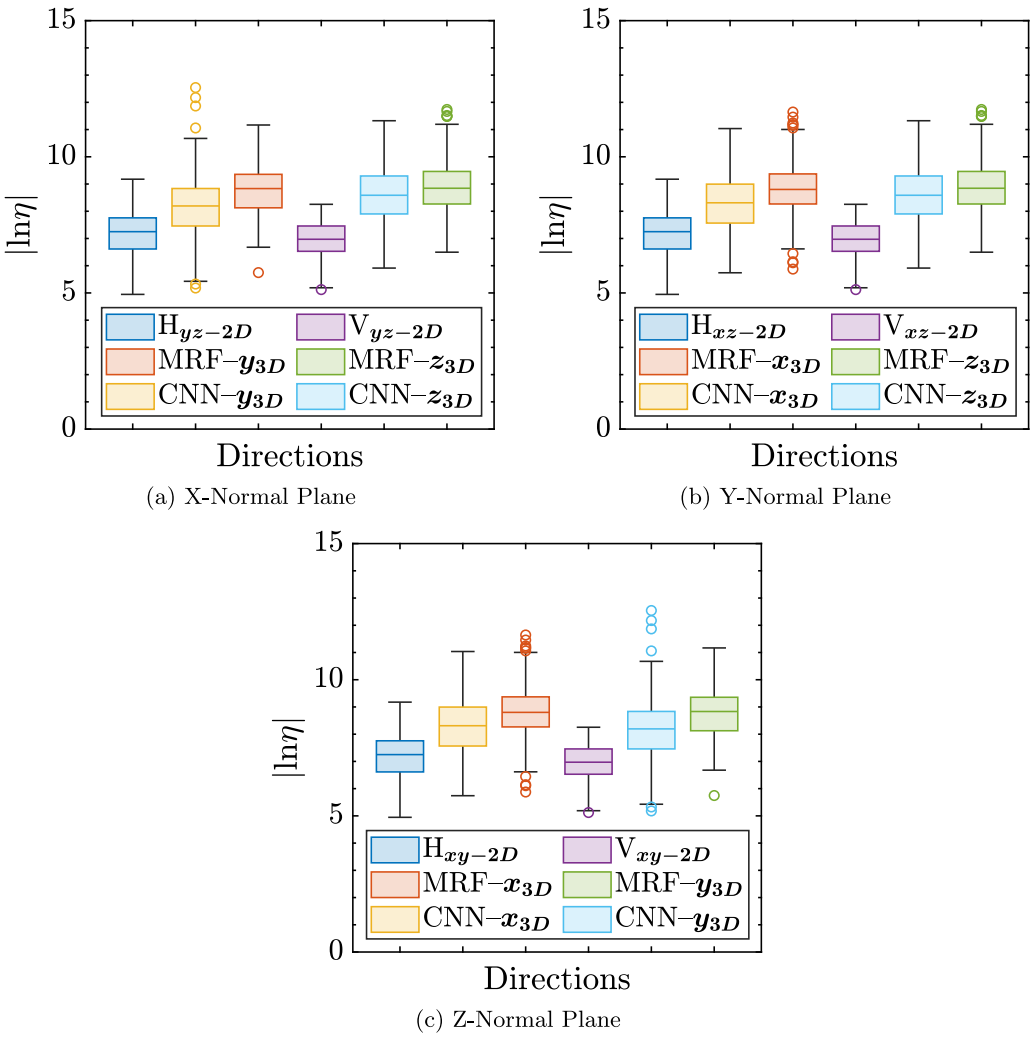

Fig. 7. Comparison of moment invariants of conventionally forged Ti-7Al microstructures generated using both MRF and CNN-based methodologies across three orthogonal planes; validated against exemplar. The data compares 2D (exemplar) against reconstructed 3D volumes. H and V denote the measured normalized variance along horizontal and vertical directions, respectively, of the exemplar.

The top-1 accuracy indicates the number of times a given deep learning model predicted the correct label with the highest probability on the ImageNet dataset. The top-1 accuracy of the VGG-19 network employed in this study is 75.2% [36].

As illustrated in this study, the CNN-based reconstruction methodology successfully generated realistic 3D solid textures for two distinct target 2D exemplars (of two distinct material systems) captured at various oblique angles. From the reconstructed virtual volumes (Fig. 4), it is evident that entire blocks of voxels that are similar to the respective texture exemplar(s) were generated. The CNN-based methodology utilized here is fully automated, and was able to produce the volumes in a single pass, contrary to the conventional global optimization-based strategy that requires high computation times. Furthermore, by minimizing the perceptual slice-based loss function (Eq. (4)) during training, computational complexity was reduced as only slices of the synthesized volume were compared to the exemplar(s). The training with a learning rate 0.1 was performed using 1 GPU (NVIDIA Quadro RTX 5000) and took ~ 2.23H for forged and 3.26H for the additively manufactured alloy, respectively. This deep learning-based microstructure reconstruction approach is material system-independent and is thus able to reproduce a diverse range of heterogeneous textures that enhances their applicability to a variety of microstructures.

5. Conclusions

AI-based reconstruction methodologies, especially deep learning-based algorithms are widely being adapted in the computational materials domain to study specific properties using advanced numerical models. Although such AI-based 2D to 3D microstructure reconstruction methodologies are ubiquitously being adopted, a proper validation procedure that explicitly quantifies the grain shapes remains unexplored in most of the works. This study serves to address this research gap and presents an application of two distinct AI-based algorithms for microstructure characterization and reconstruction of unique polycrystalline material systems with complex grain morphology. Here, we investigated two distinct reconstruction algorithms using two unique material systems and evaluated their performance characteristics, both qualitatively and quantitatively. As noted, there does not exist any guideline yet to validate the 3D synthetic complex grain shapes obtained from various algorithms. Therefore, the moment invariants-based validation procedure previously developed for 2D to 2D grain shape comparison [96] was expanded here to 3D microstructures. The developed procedure serves as a metric to gain a deeper understanding of these synthesized data as well as evaluate the statistical equivalency of the microstructure. Furthermore, the validation procedure presented in this work is universally applicable to any 2D to 3D shape comparison.

A few major conclusions are as follows:

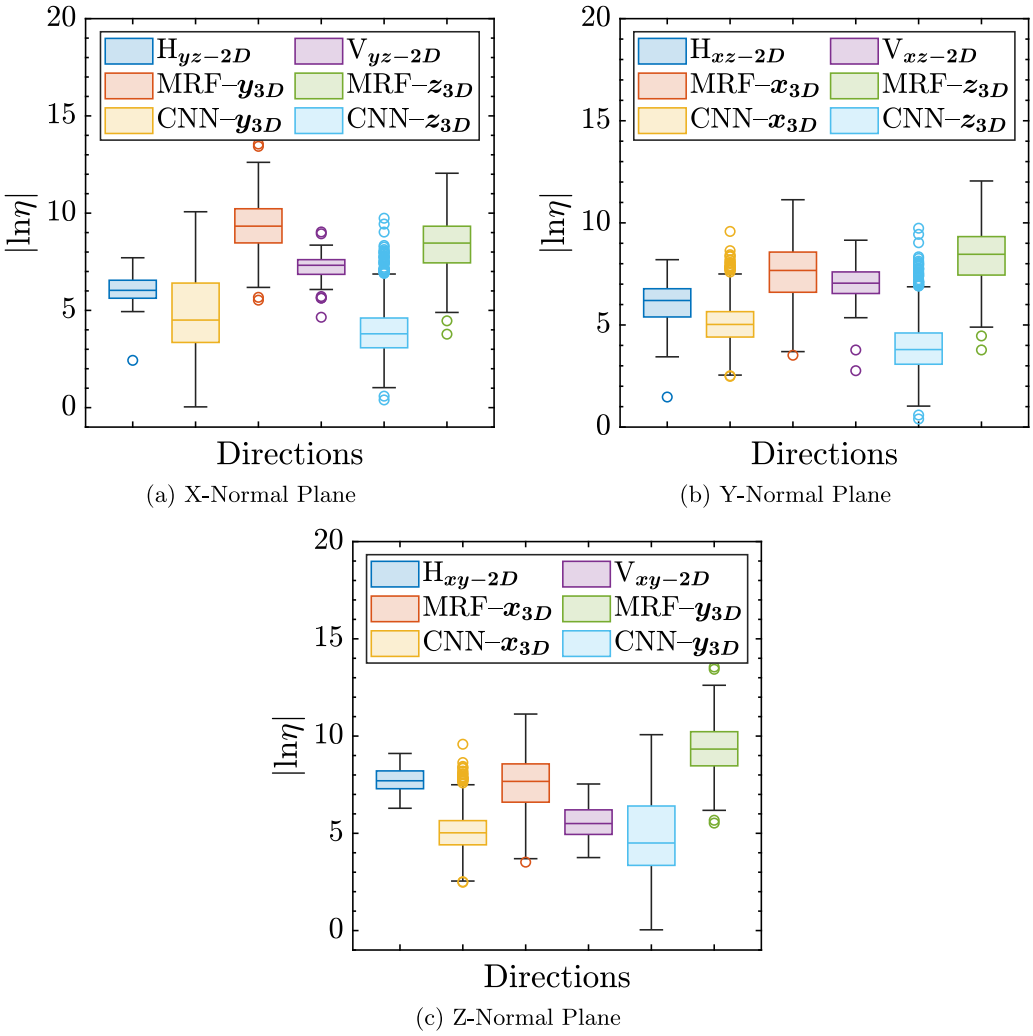

Fig. 8. Comparison of moment invariants of additively manufactured 316L stainless steel microstructures generated using both MRF and CNN-based methodologies across three orthogonal planes; validated against exemplar. H and V denote the measured normalized variance along horizontal and vertical directions, respectively, of the exemplar.

- The MRF and CNN-based reconstruction algorithms considered in this study were able to generate consistent virtual microstructure volumes for both forged and additively manufactured samples. In the case of the latter, three representative exemplars obtained along the principal orthogonal planes served as target images. Qualitative and quantitative assessments for both algorithms confirmed the successful representation of unique grain orientations across all material systems.
- Quantitative evaluations were performed using the normalized central moments (η) that are invariant to various transformations of the grain shape. The parameter η, statistically represents the normalized variance in a particular direction both in two and three dimensions. Therefore, η is a suitable metric for comparing any 2D to 3D shapes. Furthermore, the η based box whisker plots are an apt measure to study the quality of any reconstruction algorithm.
- The CNN-based reconstruction exhibited unique checker effects that are characteristic of any texture synthesis algorithm. Hence, when evaluated using the moment invariant, η, more outliers were observed than the MRF algorithm. In the anisotropic reconstruction case of the 316L stainless steel sample, the CNN-based model yielded more η outliers compared to the MRF model. However, for the isotropic reconstruction of the Ti-7Al sample using the CNN-based approach, the η values were comparatively lower and the median was closer to that of the exemplar. Hence, considering computational efficiency, the CNN-based approach can be readily adopted to create ensembles of 3D microstructures for forged samples.
- For the CNN-based model, the chosen initial learning rate of 0.1 with three slicing directions produced optimal results. A sensitivity study based on hyperparameter tuning is avoided here; alternatively, a multi-step scheduler was implemented that decayed the learning rate that led to faster convergence.

In the future, combining the advantages of both models to improve the efficacy of reconstructed microstructures will be investigated. For instance, the loss function of the CNN-based model can be modified to include the moment invariants. Furthermore, the uncertainty associated with both machine learning and deep learning-based algorithms will be also compared.

Code availability

The codes for image analysis and reconstruction used in this study are available from the corresponding author upon reasonable request.

CRediT authorship contribution statement

Arulmurugan Senthilnathan: Conceptualization, Investigation, Methodology, Writing – original draft, Writing – review & editing.

Vishnu Saseendran: Conceptualization, Investigation, Methodology, Writing – original draft, Writing – review & editing. **Pinar Acar:** Funding acquisition, Methodology, Project administration, Supervision, Writing – original draft, Writing – review & editing. **Namiko Yamamoto:** Funding acquisition, Methodology, Project administration, Writing – original draft. **Veera Sundararaghavan:** Funding acquisition, Project administration, Writing – original draft.

Declaration of competing interest

The authors declare that they have no known competing financial interests or personal relationships that could have appeared to influence the work reported in this paper.

Acknowledgments

Penn State co-authors acknowledge the support of NASA's Physical Sciences Research Program (80NSSC22K0083) and Penn State Institute for Computational and Data Sciences RISE Seed Grant. V.S. acknowledges the support of AFOSR awards FA9550-22-1-0319 and FA9550-18-1-0091 for the MRFVoxel code development. Virginia Tech co-authors acknowledge support from AFOSR YIP award FA9550-21-1-0120 and NSF CMMI award #2053840.

References

[1] C. Yeong, S. Torquato, Reconstructing random media, Phys. Rev. E 57 (1) (1998) 495.
[2] Z. Liang, C. Fernandes, F. Magnani, P. Philippi, A reconstruction technique for three-dimensional porous media using image analysis and Fourier transforms, J. Pet. Sci. Eng. 21 (3–4) (1998) 273–283.
[3] Y. Ju, J. Zheng, M. Epstein, L. Sudak, J. Wang, X. Zhao, 3D numerical reconstruction of well-connected porous structure of rock using fractal algorithms, Comput. Methods Appl. Mech. Engrg. 279 (2014) 212–226.
[4] J. Feng, C. Li, S. Cen, D. Owen, Statistical reconstruction of two-phase random media, Comput. Struct. 137 (2014) 78–92.
[5] A. Hajizadeh, A. Safekordi, F.A. Farhadpour, A multiple-point statistics algorithm for 3D pore space reconstruction from 2D images, Adv. Water Resour. 34 (10) (2011) 1256–1267.
[6] Y. Wu, C. Lin, L. Ren, W. Yan, S. An, B. Chen, Y. Wang, X. Zhang, C. You, Y. Zhang, Reconstruction of 3D porous media using multiple-point statistics based on a 3D training image, J. Nat. Gas Sci. Eng. 51 (2018) 129–140.
[7] K. Wu, M.I. Van Dijke, G.D. Couples, Z. Jiang, J. Ma, K.S. Sorbie, J. Crawford, I. Young, X. Zhang, 3D stochastic modelling of heterogeneous porous media–applications to reservoir rocks, Transp. Porous Media 65 (2006) 443–467.
[8] C. Wang, X. Tan, S.B. Tor, C. Lim, Machine learning in additive manufacturing: State-of-the-art and perspectives, Addit. Manuf. 36 (2020) 101538.
[9] P. Seibert, A. Raßloff, K.A. Kalina, J. Gussone, K. Bugelnig, M. Diehl, M. Kästner, Two-stage 2D-to-3D reconstruction of realistic microstructures: Implementation and numerical validation by effective properties, Comput. Methods Appl. Mech. Engrg. 412 (2023) 116098.
[10] A. Adam, F. Wang, X. Li, Efficient reconstruction and validation of heterogeneous microstructures for energy applications, Int. J. Energy Res. 46 (15) (2022) 22757–22771.
[11] X. Li, Y. Zhang, H. Zhao, C. Burkhart, L.C. Brinson, W. Chen, A transfer learning approach for microstructure reconstruction and structure-property predictions, Sci. Rep. 8 (1) (2018) 13461.
[12] Y. Liu, M.S. Greene, W. Chen, D.A. Dikin, W.K. Liu, Computational microstructure characterization and reconstruction for stochastic multiscale material design, Comput. Aided Des. 45 (1) (2013) 65–76.
[13] H. Xu, C. Bae, Stochastic 3D microstructure reconstruction and mechanical modeling of anisotropic battery separators, J. Power Sources 430 (2019) 67–73.
[14] A. Senthilnathan, P. Acar, M. De Graef, Markov random field based microstructure reconstruction using the principal image moments, Mater. Charact. 178 (2021) 111281.
[15] A. Kumar, L. Nguyen, M. DeGraef, V. Sundararaghavan, A Markov random field approach for microstructure synthesis, Modelling Simul. Mater. Sci. Eng. 24 (3) (2016) 035015.
[16] J. Gutierrez, J. Rabin, B. Galerne, T. Hurtut, On demand solid texture synthesis using deep 3D networks, Comput. Graph. Forum 39 (2020) 511–530.
[17] X. Liu, V. Shapiro, Random heterogeneous materials via texture synthesis, Comput. Mater. Sci. 99 (2015) 177–189.
[18] V. Sundararaghavan, Reconstruction of three-dimensional anisotropic microstructures from two-dimensional micrographs imaged on orthogonal planes, Integr. Mater. Manuf. Innov. 3 (2014) 240–250.
[19] D.M. Turner, S.R. Kalidindi, Statistical construction of 3-D microstructures from 2-D exemplars collected on oblique sections, Acta Mater. 102 (2016) 136–148.
[20] S.-Y. Kim, J.-S. Kim, J.H. Lee, J.H. Kim, T.-S. Han, Comparison of microstructure characterization methods by two-point correlation functions and reconstruction of 3D microstructures using 2D TEM images with high degree of phase clustering, Mater. Charact. 172 (2021) 110876.
[21] E. Levina, P.J. Bickel, Texture synthesis and nonparametric resampling of random fields, Ann. Statist. 34 (4) (2006) 1751–1773.
[22] B.A. Cipra, An introduction to the Ising model, Amer. Math. Monthly 94 (10) (1987) 937–959.
[23] I. Javaheri, V. Sundararaghavan, Polycrystalline microstructure reconstruction using Markov random fields and histogram matching, Comput. Aided Des. 120 (2020) 102806.
[24] I. Javaheri, M.T. Andani, V. Sundararaghavan, Large-scale synthesis of metal additively-manufactured microstructures using markov random fields, Comput. Mater. Sci. 206 (2022) 111228.
[25] B.L. DeCost, T. Francis, E.A. Holm, Exploring the microstructure manifold: image texture representations applied to ultrahigh carbon steel microstructures, Acta Mater. 133 (2017) 30–40.
[26] N. Lubbers, T. Lookman, K. Barros, Inferring low-dimensional microstructure representations using convolutional neural networks, Phys. Rev. E 96 (5) (2017) 052111.
[27] R. Bostanabad, Reconstruction of 3D microstructures from 2D images via transfer learning, Comput. Aided Des. 128 (2020) 102906.
[28] A. Bhaduri, A. Gupta, A. Olivier, L. Graham-Brady, An efficient optimization based microstructure reconstruction approach with multiple loss functions, Comput. Mater. Sci. 199 (2021) 110709.
[29] H. Zhang, T. Xu, H. Li, S. Zhang, X. Wang, X. Huang, D.N. Metaxas, Stackgan: Text to photo-realistic image synthesis with stacked generative adversarial networks, in: Proceedings of the IEEE International Conference on Computer Vision, 2017, pp. 5907–5915.
[30] A. Dosovitskiy, J.T. Springenberg, M. Tatarchenko, T. Brox, Learning to generate chairs, tables and cars with convolutional networks, IEEE Trans. Pattern Anal. Mach. Intell. 39 (4) (2016) 692–705.
[31] X. Zhao, J. Guo, L. Wang, F. Li, J. Zheng, B. Yang, STS-GAN: Can we synthesize solid texture with high fidelity from arbitrary exemplars? 2021, arXiv preprint arXiv:2102.03973.
[32] T. Portenier, S. Arjomand Bigdeli, O. Goksel, Gramgan: Deep 3D texture synthesis from 2D exemplars, Adv. Neural Inf. Process. Syst. 33 (2020) 6994–7004.
[33] J. Fu, D. Xiao, D. Li, H.R. Thomas, C. Li, Stochastic reconstruction of 3D microstructures from 2D cross-sectional images using machine learning-based characterization, Comput. Methods Appl. Mech. Engrg. 390 (2022) 114532.
[34] R. Cang, Y. Xu, S. Chen, Y. Liu, Y. Jiao, M. Yi Ren, Microstructure representation and reconstruction of heterogeneous materials via deep belief network for computational material design, J. Mech. Des. 139 (7) (2017) 071404.
[35] X. Li, Z. Yang, L.C. Brinson, A. Choudhary, A. Agrawal, W. Chen, A deep adversarial learning methodology for designing microstructural material systems, in: International Design Engineering Technical Conferences and Computers and Information in Engineering Conference, Vol. 51760, American Society of Mechanical Engineers, 2018, V02BT03A008.
[36] K. Simonyan, A. Zisserman, Very deep convolutional networks for large-scale image recognition, 2014, arXiv preprint arXiv:1409.1556.
[37] J. Deng, A large-scale hierarchical image database, Proc. IEEE Comput. Vis. Pattern Recognit., 2009 (2009).
[38] D.R. Peachey, Solid texturing of complex surfaces, in: Proceedings of the 12th Annual Conference on Computer graphics and Interactive Techniques, 1985, pp. 279–286.
[39] K. Perlin, An image synthesizer, ACM Siggraph Comput. Graph. 19 (3) (1985) 287–296.
[40] J. Kopf, C.-W. Fu, D. Cohen-Or, O. Deussen, D. Lischinski, T.-T. Wong, Solid texture synthesis from 2D exemplars, ACM Trans. Graph. (Proc. SIGGRAPH 2007) 26 (3) (2007) 2:1–2:9.
[41] N. Pietroni, P. Cignoni, M. Otaduy, R. Scopigno, Solid-texture synthesis: A survey, IEEE Comput. Graph. Appl. 30 (4) (2010) 74–89.
[42] J. Chen, B. Wang, High quality solid texture synthesis using position and index histogram matching, Vis. Comput. 26 (2010) 253–262.
[43] S. Zirek, Synthesising 3d solid models of natural heterogeneous materials from single sample image, using encoding deep convolutional generative adversarial networks, Syst. Soft Comput. 5 (2023) 200051.
[44] S. Kench, S.J. Cooper, Generating three-dimensional structures from a two-dimensional slice with generative adversarial network-based dimensionality expansion, Nat. Mach. Intell. 3 (4) (2021) 299–305.
[45] F. Zhang, Q. Teng, H. Chen, X. He, X. Dong, Slice-to-voxel stochastic reconstructions on porous media with hybrid deep generative model, Comput. Mater. Sci. 186 (2021) 110018.
[46] V. Saseendran, N. Yamamoto, P. Collins, A. Radlinska, E.J. Pineda, B.A. Bednarcyk, Reconstruction of tricalcium silicate microstructures for repeating unit cell analysis, in: AIAA Scitech 2023 Forum, 2023, p. 2025.
[47] X. Zhao, X. Wu, L. Wang, P. Hou, Q. Li, Y. Zhang, B. Yang, Three-dimensional microstructural image synthesis from 2D backscattered electron image of cement paste, 2022, arXiv preprint arXiv:2204.01645.

[48] H. Xiao, L. He, Y. Zheng, S. Yan, 3D solid digital and numerical modeling of multimineral heterogeneous rocks based on deep learning, Geomech. Geophys. Geo-Energy Geo-Resour. 8 (6) (2022) 188.
[49] V. Saseendran, N. Yamamoto, I. Kaleel, E.J. Pineda, B.A. Bednarcyk, P. Collins, A. Radlinska, Multiscale modeling of reconstructed tricalcium silicate using NASA multiscale analysis tool, in: AIAA SCITECH 2024 Forum, 2024, p. 1001.
[50] V. Saseendran, N. Yamamoto, P.J. Collins, A. Radlińska, S. Mueller, E.M. Jackson, Unlocking the potential: analyzing 3D microstructure of small-scale cement samples from space using deep learning, npj Microgravity 10 (1) (2024) 11.
[51] I. Goodfellow, J. Pouget-Abadie, M. Mirza, B. Xu, D. Warde-Farley, S. Ozair, A. Courville, Y. Bengio, Generative adversarial nets, Adv. Neural Inf. Process. Syst. 27 (2014).
[52] M. Sahimi, P. Tahmasebi, Reconstruction, optimization, and design of heterogeneous materials and media: Basic principles, computational algorithms, and applications, Phys. Rep. 939 (2021) 1–82.
[53] L. Mosser, O. Dubrule, M.J. Blunt, Reconstruction of three-dimensional porous media using generative adversarial neural networks, Phys. Rev. E 96 (4) (2017) 043309.
[54] S. Kench, S.J. Cooper, Generating three-dimensional structures from a two-dimensional slice with generative adversarial network-based dimensionality expansion, Nat. Mach. Intell. 3 (4) (2021) 299–305.
[55] Y. Li, P. Jian, G. Han, Cascaded progressive generative adversarial networks for reconstructing three-dimensional grayscale core images from a single two-dimensional image, Front. Phys. 10 (2022) 716708.
[56] T. Hsu, W.K. Epting, H. Kim, H.W. Abernathy, G.A. Hackett, A.D. Rollett, P.A. Salvador, E.A. Holm, Microstructure generation via generative adversarial network for heterogeneous, topologically complex 3D materials, Jom 73 (2021) 90–102.
[57] Z. Yang, X. Li, L. Catherine Brinson, A.N. Choudhary, W. Chen, A. Agrawal, Microstructural materials design via deep adversarial learning methodology, J. Mech. Des. 140 (11) (2018) 111416.
[58] A. Henkes, H. Wessels, Three-dimensional microstructure generation using generative adversarial neural networks in the context of continuum micromechanics, Comput. Methods Appl. Mech. Engrg. 400 (2022) 115497.
[59] Y. Li, P. Jian, G. Han, Cascaded progressive generative adversarial networks for reconstructing three-dimensional grayscale core images from a single two-dimensional image, Front. Phys. 10 (2022) 716708.
[60] J. Feng, Q. Teng, X. He, X. Wu, Accelerating multi-point statistics reconstruction method for porous media via deep learning, Acta Mater. 159 (2018) 296–308.
[61] B. Murgas, J. Stickel, S. Ghosh, Generative adversarial network (GAN) enabled statistically equivalent virtual microstructures (SEVM) for modeling cold spray formed bimodal polycrystals, npj Comput. Mater. 10 (1) (2024) 32.
[62] D.K. Jangid, N.R. Brodnik, A. Khan, M.G. Goebel, M.P. Echlin, T.M. Pollock, S.H. Daly, B. Manjunath, 3D grain shape generation in polycrystals using generative adversarial networks, Integr. Mater. Manuf. Innov. 11 (1) (2022) 71–84.
[63] S. Lala, M. Shady, A. Belyaeva, M. Liu, Evaluation of mode collapse in generative adversarial networks, High Perform. Extrem. Comput. (2018).
[64] L. Metz, B. Poole, D. Pfau, J. Sohl-Dickstein, Unrolled generative adversarial networks, 2016, arXiv preprint arXiv:1611.02163.
[65] M. Arjovsky, L. Bottou, Towards principled methods for training generative adversarial networks, 2017, arXiv preprint arXiv:1701.04862.
[66] Y. Zhang, P. Seibert, A. Otto, A. Raßloff, M. Ambati, M. Kästner, DA-VEGAN: Differentiably Augmenting VAE-GAN for microstructure reconstruction from extremely small data sets, Comput. Mater. Sci. 232 (2024) 112661.
[67] X. Lyu, X. Ren, Microstructure reconstruction of 2D/3D random materials via diffusion-based deep generative models, Sci. Rep. 14 (1) (2024) 5041.
[68] S. Bond-Taylor, A. Leach, Y. Long, C.G. Willcocks, Deep generative modelling: A comparative review of vaes, gans, normalizing flows, energy-based and autoregressive models, IEEE Trans. Pattern Anal. Mach. Intell. 44 (11) (2021) 7327–7347.
[69] R. Shams, M. Masihi, R.B. Boozarjomehry, M.J. Blunt, Coupled generative adversarial and auto-encoder neural networks to reconstruct three-dimensional multi-scale porous media, J. Pet. Sci. Eng. 186 (2020) 106794.
[70] F. Zhang, Q. Teng, H. Chen, X. He, X. Dong, Slice-to-voxel stochastic reconstructions on porous media with hybrid deep generative model, Comput. Mater. Sci. 186 (2021) 110018.
[71] R. Mukherjee, F. Sauvage, H. Xie, R. Löw, F. Mintert, Preparation of ordered states in ultra-cold gases using bayesian optimization, New J. Phys. 22 (7) (2020) 075001.
[72] H. Chamani, A. Rabbani, K.P. Russell, A.L. Zydney, E.D. Gomez, J. Hattrick-Simpers, J.R. Werber, Data-science-based reconstruction of 3-D membrane pore structure using a single 2-D micrograph, J. Membr. Sci. 678 (2023) 121673.
[73] A. Raßloff, P. Seibert, K.A. Kalina, M. Kästner, Inverse design of spinodoid structures using Bayesian optimization, 2024, arXiv preprint arXiv:2402.13054.
[74] N. Kusampudi, M. Diehl, Inverse design of dual-phase steel microstructures using generative machine learning model and Bayesian optimization, Int. J. Plast. 171 (2023) 103776.
[75] S.H. Scheres, A Bayesian view on cryo-EM structure determination, J. Mol. Biol. 415 (2) (2012) 406–418.
[76] S.H. Scheres, RELION: implementation of a Bayesian approach to cryo-EM structure determination, J. Struct. Biol. 180 (3) (2012) 519–530.
[77] C.B. Clement, J.P. Sethna, K.C. Nowack, Reconstruction of current densities from magnetic images by Bayesian inference, 2019, arXiv preprint arXiv:1910.12929.
[78] Y. Xu, C.W. Farris, S.W. Anderson, X. Zhang, K.A. Brown, Bayesian reconstruction of magnetic resonance images using Gaussian processes, Sci. Rep. 13 (1) (2023) 12527.
[79] C. Düreth, P. Seibert, D. Rücker, S. Handford, M. Kästner, M. Gude, Conditional diffusion-based microstructure reconstruction, Mater. Today Commun. 35 (2023) 105608.
[80] K.-H. Lee, G.J. Yun, Microstructure reconstruction using diffusion-based generative models, Mech. Adv. Mater. Struct. (2023) 1–19.
[81] E. Azqadan, H. Jahed, A. Arami, Predictive microstructure image generation using denoising diffusion probabilistic models, Acta Mater. 261 (2023) 119406.
[82] P. Fernandez-Zelaia, J. Cheng, J. Mayeur, A.K. Ziabari, M.M. Kirka, Digital polycrystalline microstructure generation using diffusion probabilistic models, Materialia 33 (2024) 101976.
[83] X. Lyu, X. Ren, Microstructure reconstruction of 2D/3D random materials via diffusion-based deep generative models, Sci. Rep. 14 (1) (2024) 5041.
[84] K.-H. Lee, G.J. Yun, Denoising diffusion-based synthetic generation of three-dimensional (3D) anisotropic microstructures from two-dimensional (2D) micrographs, Comput. Methods Appl. Mech. Engrg. 423 (2024) 116876.
[85] R. Bostanabad, A.T. Bui, W. Xie, D.W. Apley, W. Chen, Stochastic microstructure characterization and reconstruction via supervised learning, Acta Mater. 103 (2016) 89–102.
[86] A. Senthilnathan, I. Javaheri, H. Zhao, V. Sundararaghavan, M. DeGraef, P. Acar, Uncertainty quantification of metallic microstructures using principal image moments, Comput. Mater. Sci. 215 (2022) 111775.
[87] J. MacSleyne, M. Uchic, J. Simmons, M. De Graef, Three-dimensional analysis of secondary γ' precipitates in René-88 DT and UMF-20 superalloys, Acta Mater. 57 (20) (2009) 6251–6267.
[88] P. Callahan, M. Groeber, M. De Graef, Towards a quantitative comparison between experimental and synthetic grain structures, Acta Mater. 111 (2016) 242–252.
[89] J. Chen, B. Wang, High quality solid texture synthesis using position and index histogram matching, Vis. Comput. 26 (2010) 253–262.
[90] R. Harrison, E.A. Holm, M. De Graef, On the use of 2D moment invariants in the classification of additive manufacturing powder feedstock, Mater. Charact. 149 (2019) 255–263.
[91] J. MacSleyne, J. Simmons, M. De Graef, On the use of 2-D moment invariants for the automated classification of particle shapes, Acta Mater. 56 (3) (2008) 427–437.
[92] J. MacSleyne, J. Simmons, M. De Graef, On the use of moment invariants for the automated analysis of 3D particle shapes, Modelling Simul. Mater. Sci. Eng. 16 (4) (2008) 045008.
[93] L. Gatys, A.S. Ecker, M. Bethge, Texture synthesis using convolutional neural networks, Adv. Neural Inf. Process. Syst. 28 (2015).
[94] D.P. Kingma, J. Ba, Adam: A method for stochastic optimization, 2015, arXiv preprint arXiv:1412.6980, 9.
[95] M.-K. Hu, Visual pattern recognition by moment invariants, IRE Trans. Inf. Theory 8 (2) (1962) 179–187.
[96] A. Senthilnathan, I. Javaheri, V. Sundararaghavan, P. Acar, Computational characterization and model verification for 3D microstructure reconstruction of additively manufactured materials, in: AIAA SciTech 2023 Forum, AIAA, 2023.